Immiscible Two-Phase Flow in Porous Media: Effective Rheology in the Continuum Limit

Subhadeep Roy[1] · **Santanu Sinha[2]** · **Alex Hansen[3]**

Abstract

We consider steady-state immiscible and incompressible two-phase flow in porous media. It is becoming increasingly clear that there is a flow regime where the volumetric flow rate depends on the pressure gradient as a power law with an exponent larger than one. This occurs when the capillary forces and viscous forces compete. At higher flow rates, where the viscous forces dominate, the volumetric flow rate depends linearly on the pressure gradient. This means that there is a crossover pressure gradient that separates these two flow regimes. At small enough pressure gradient, the capillary forces dominate. If one or both of the immiscible fluids percolate, the volumetric flow rate will then depend linearly on the pressure gradient as the interfaces will not move. If none of the fluids percolate, there will be a minimum pressure gradient threshold to mobilize the interfaces and thereby get the fluids moving. We now imagine a core sample of a given size. The question we pose is what happens to the crossover pressure gradient that separates the power-law regime from the high-flow rate linear regime and the threshold pressure gradient that blocks the flow at low pressure gradients when the size of the core sample is increased. Based on analytical calculations using the capillary bundle model and on numerical simulations using a dynamical pore-network model, we find that the crossover pressure gradient and the threshold pressure gradient decrease with two distinct power laws in the size. This means that the power-law regime disappears in the continuum limit where the pores are infinitely small compared to the sample size.

✉ Subhadeep Roy
  subhadeep.r@hyderabad.bits-pilani.ac.in

  Santanu Sinha
  santanu.sinha@ntnu.no

  Alex Hansen
  alex.hansen@ntnu.no

[1] Department of Physics, Birla Institute of Technology and Science Pilani, Hyderabad Campus, Secunderabad, Telangana 500078, India

[2] PoreLab, Department of Physics, University of Oslo, 0316 Oslo, Norway

[3] PoreLab, Department of Physics, Norwegian University of Science and Technology, 7491 Trondheim, Norway

1 Introduction

In 1856, Darcy published his famous treatise where he formulated the linear relationship between volumetric flow rate and pressure drop in a porous column, i.e., the Darcy law (Darcy 1856). Eighty years later, the Darcy law was generalized to the simultaneous flow of two immiscible fluids by Wyckoff and Botset (1936). The basic idea behind this generalization was that each fluid sees an available space in which it can flow consisting of the total pore space minus the space the other fluid occupies. Each fluid is then assumed to obey the Darcy law within this diminished pore space. This idea is clearly oversimplified. It remains to date, however with some important addenda such as the incorporation of capillary effects (Leverett 1941), the dominating tool for simulations of immiscible two-phase flow in porous media. This is in spite of numerous attempts over the years at improving this approach or substitute it for an entirely new approach (Hassanizadeh and Gray 1990, 1993a, b; Niessner et al. 2011; Gray and Miller 2014; Kjelstrup et al. 2018, 2019; Hilfer and Besserer 2000; Hilfer 2006a, b, c; Hilfer and Doster 2009; Doster et al. 2012; Valavanides et al. 1998; Valavanides 2012, 2018; Hansen et al. 2018; Roy et al. 2020, 2022; Hansen et al. 2023; Pedersen and Hansen 2023; Fyhn et al. 2023).

A simpler question may be posed when generalizing the Darcy equation to immiscible two-phase flow in porous media. Rather than asking for the flow rate of each of the two fluids, how does the *combined flow* react to a given pressure drop? It has since Tallakstad et al. (2009a, 2009b) did their experimental study of immiscible two-phase flow under steady-state conditions, become increasingly clear that there is a flow regime in which the flow rate is proportional to the pressure drop to a power larger than one (Grøva and Hansen 2011; Rassi et al. 2011; Sinha and Hansen 2012; Sinha et al. 2017; Yiotis et al. 2019; Gao et al. 2020; Zhang et al. 2021; Fyhn et al. 2021; Zhang et al. 2022; Fyhn et al. 2023).

In the experimental setups that have been used, the flow rate of each fluid into the porous medium is controlled and the pressure drop across the porous medium is measured. This leads to the two fluids simultaneously percolating at very low flow rates where the capillary forces are too strong for the viscous forces to move the fluid interfaces. This results in the standard linear Darcy law prevailing. As the flow rates are increased, Gao et al. (2020) report a regime occurring where there are strong pressure fluctuations but still the linear Darcy law is seen. This is when the interfaces start being mobilized. Then, at even higher flow rates, nonlinearity sets in, and a power-law relation between flow rate and pressure drop is measured. This power law may be associated with the gradual increase in the number of mobilized interfaces as the flow rates increase (Tallakstad et al. 2009b; Sinha and Hansen 2012). Lastly, at very high flow rates, the capillary forces become negligible compared to the viscous forces, and again, the system reverts to obey a linear Darcy law (Sinha et al. 2017).

A simplified problem compared to that of immiscible two-phase flow in porous media is that of bubbles flowing in a single tube (Sinha et al. 2011; Xu and Wang 2014; Lanza et al. 2022; Cheon et al. 2023). Sinha et al. (2011) studied a bubble train in a tube with a variable radius assuming no fluid films forming as a function of imposed pressure drop along the tube. They found that the time-averaged volumetric flow rate depends on the square root of the *excess pressure drop,* that is the pressure drop along the tube minus a depinning or threshold pressure P_t. Xu and Wang (2014) also identified a threshold pressure in their numerical simulations. However, this threshold pressure has a different character from that in the previous study: It is the pressure drop at which contact lines start mobilizing. The movement of the contact lines consumes energy leading to the effective permeability drop.

Xu and Wang (2014) suggest that this is the main mechanism responsible for the nonlinearity in the flow-pressure relationship. Lanza et al. considered an immiscible mixture of a non-Newtonian and a Newtonian fluid moving along the tube (Lanza et al. 2022); whereas, Cheon et al. considered a mixture of compressible and incompressible fluids moving along the tube (Cheon et al. 2023), both with pressure drop as control variable. In both cases, a non-trivial power law dependence between the flow rate and pressure drop were found.

The question of whether there should be a threshold pressure or not in the power-law regime is an important one as assuming there to be one may alter significantly the measured value of the exponent β seen in the power-law regime where

$$Q \sim \begin{cases} 0 \,, & \text{if } |\Delta P| \leq P_t \,, \\ (|\Delta P| - P_t)^\beta \,, & \text{if } P_t < |\Delta P| \leq P_M \,, \\ |\Delta P| \,, & \text{if } P_M < |\Delta P| \,, \end{cases} \qquad (1)$$

where $Q = Q_w + Q_n$ is the volumetric flow rate consisting of the sum of volumetric flow rates of the wetting fluid Q_w, and the non-wetting fluid Q_n. ΔP is the pressure drop across the sample.

The third flow regime in this equation appears when the viscous forces dominate the capillary forces, leading to a linear relationship between volumetric flow rate and the pressure drop. P_M is the crossover pressure drop that distinguishes the power-law regime from the linear high-pressure drop regime.

The value of β varies in the literature. Tallakstad et al. (2009a, 2009b) reported $\beta = 1/0.54 = 1.85$ (in these papers the inverse exponent was reported), Rassi et al. (2011) reported a range of values, $\beta = 1/0.3 = 3.3$ to $\beta = 1/0.45 = 2.2$, and Gao et al. (2020) reported $\beta = 1/0.6 = 1.67$. These results are based on experiments and they all assume $P_t = 0$. Sinha et al. (2017) report for their experiments $\beta = 1/0.46 = 2.2$, based on there is a threshold. Sinha and Hansen (2012) in numerical work also assumes a threshold pressure based on a dynamic pore-network simulator (Joekar-Niasar and Hassanizadeh 2012), where fluid interfaces are moved according to the forces they experience (Aker et al. 1998; Gjennestad et al. 2018; Sinha et al. 2020; Zhao et al. 2019), and found $\beta = 1/0.51 = 2.0$. The network representing the porous medium was here square lattice with disorder in the radii of the pore throats. They followed this up with an effective medium calculation yielding $\beta = 2$. Sinha et al. (2017) reported $\beta = 1/0.50 = 2.0$ to $\beta = 1/0.54 = 1.85$ based on numerical studies with reconstructed porous media using the same numerical model as in Sinha and Hansen (2012). Yiotis et al. (2019) proposed $\beta = 3/2$ based on numerical work and assuming the existence of a threshold pressure. Recently Fyhn et al. (2023) have studied a pore-network model for a mixture of grains with opposite wetting properties with respect to the two immiscible fluids. Depending on the filling ratio between the two grain types, there is a regime where there is no threshold pressure. They find an exponent $\beta = 2.56$ in this regime.

A note of caution on the threshold pressure: There is a lesson to be learned from the study of a very different problem. In 1993 Måløy et al. (1993) published an experimental study where a rough hard surface was pressed into a soft material with a flat surface, measuring the force as a function of the deformation. At first contact, the Hertz contact law was seen, i.e., the force depended on the deformation to the 3/2 power. As the deformation proceeded, a different power law emerged, however not in the deformation but in the deformation minus a threshold deformation. And here is the lesson: The threshold deformation was *not* the deformation at first contact where the Hertz contact law was seen. Transferring this

result to the power law Darcy case, our point is that the threshold pressure that shows up in the power law does *not* have to be the pressure needed to get the fluids flowing. The power law (1) may be followed down to a certain pressure difference larger than P_t. At this pressure difference, there may then be a crossover to a different regime controlled by different physics, e.g., a linear one as Gao et al. (2020) reported.

We will here discuss another aspect of the power-law flow regime which so far has not been touched upon. Up to now, the system sizes that have been used in establishing the existence of the power-law regime, even if the details have not yet been sorted out, have been fixed. This applies both to the experimental and numerical studies that have been published. What happens if we increase the system size? To be concrete, think of a core plug with a transversal area A and a length L. Increasing the system size means increasing A and L in a proportional way that does not deform the shape of the sample.

Does the threshold pressure P_t remain the same? And what about the crossover pressure drop P_M that distinguishes the regime power-law regime where the capillary and viscous forces compete, and the linear regime where the viscous forces dominate? We define the corresponding threshold pressure gradient and crossover pressure gradient

$$p_t = \frac{P_t}{L},\tag{2}$$

$$p_M = \frac{P_M}{L},\tag{3}$$

which can then be compared to the average pressure gradient $p = \Delta P/L$, where ΔP is the pressure drop across the sample. We keep p constant when L is increased. Our conclusion, based on numerical evidence from the dynamic pore-network model (Aker et al. 1998; Gjennestad et al. 2018; Sinha et al. 2020) and on analytic calculation using the capillary bundle model (Roy et al. 2019), is that both the threshold pressure gradient p_t and the crossover pressure gradient p_M, decrease with increasing L. Moreover, they follow specific but different power laws in doing so.

In the next section, we present a scaling analysis of the viscosity-dominated linear flow regime and the power-law flow regime that sets the stage for our analysis. We then turn in Sect. 3 to the capillary bundle model. Section 4 contains our numerical study based on scaling up the square lattice. The last section contains a discussion of the arguments presented earlier in the paper together with our conclusion.

2 Scaling Analysis

We assume a porous medium sample that has length L and transversal area A. If d ($= 2$ or 3) is the dimensionality of the porous sample we are considering, we have that $A \propto L^{d-1}$. There is a pressure drop ΔP across it and this generates a volumetric flow rate of Q. When the flow rate is high so that capillary forces may be neglected, the constitutive relation between Q and ΔP is given by the Darcy law,

$$Q = -M_d \Delta P,\tag{4}$$

where M_d is the mobility. We introduce the Darcy velocity

$$v = \frac{Q}{A} \, , \tag{5}$$

and the pressure gradient

$$p = \frac{\Delta P}{L} \, . \tag{6}$$

The Darcy equation then takes the form

$$v = -m_d \, p \, , \tag{7}$$

where

$$m_d = \frac{M_d L}{A} \, . \tag{8}$$

Equations (7) and (8) are both independent of the transversal area A and the length L of the sample.

As has been described in the Introduction, there is a regime in which the volumetric flow rate Q depends on the pressure drop ΔP as a power law,

$$Q = -M_\beta \, \text{sign}(\Delta P)\Theta(|\Delta P| - P_t)(|\Delta P| - P_t)^\beta \, , \tag{9}$$

where M_β is the power-law mobility and P_t is a threshold pressure. Here $\Theta(|\Delta P| - P_t)$ is the Heaviside function which is one for positive arguments and zero for negative arguments. We use the Heaviside function to mark the end of the power-law regime when the pressure drop is lowered. There may be a crossover to a different regime before reaching this lower cutoff (Gao et al. 2020). This occurs when either or both fluids percolate.

We also remind the reader of the crossover pressure drop P_M as that which separates the power law flow regime from the linear viscosity-dominated regime, see Eq. (1).

We express the power law Darcy law (9) in terms of the Darcy velocity and the pressure gradient,

$$v = -m_\beta \, \text{sign}(p)\Theta\big(|p| - p_t\big)\big(|p| - p_t\big)^\beta \, , \tag{10}$$

where we have used the definitions (2) and (3). We then have that

$$m_\beta = \frac{M_\beta L^\beta}{A} \, . \tag{11}$$

Equations (7) and (10) are then the constitutive equations relating Darcy velocity to the pressure gradient in the viscosity-dominated and in the power law flow regimes. In the viscosity-dominated regime, both the Darcy velocity and the pressure gradient are intensive variables, i.e., they do not depend on $A \propto L^{d-1}$ or L. This leads to m_d being intensive too, i.e., independent of L.

Even though the power law flow regime constitutive Eq. (10) looks intensive too, we will in the following demonstrate that it is not. The mobility m_β turns out to *increase* with increasing L as a power law, and this, in turn, leads to the crossover pressure gradient p_M *decreasing* as a power law with increasing L. By another argument, we also show that the threshold pressure gradient p_t also decreases with increasing L, also as a power law, but with a different exponent.

3 Capillary Bundle Model

In order to find the scaling properties of m_β and p_t, we consider the capillary bundle model (Scheidegger 1953, 1974). This simple model of immiscible two-phase flow in porous media is analytically tractable. Furthermore, it is surprisingly accurate when the right questions are put to it. We note that the one feature of ordinary porous media that lacks in the capillary bundle model is internal mixing. As long as mixing is not an important feature of the problem at hand, the model does well. It will turn out that the analytical results gotten from the capillary bundle model are supported by the numerical results from the dynamic pore-network model to be studied in the next section.

The capillary bundle model consists of N parallel capillary tubes of equal length L as shown in Fig. 1. The radii of the tubes vary along their lengths, creating capillary forces due to the interfaces that compete with the viscous forces.

We now focus on one of the N tubes belonging to the capillary bundle model — say we pick tube number m. We introduce a position variable x along the tubes $0 \leq x \leq L$. Following Sinha et al. (2011), we assume the radius of tube m varies as

$$r_m(x) = \frac{\bar{r}_m}{1 - b\cos(2\pi x/l)} , \tag{12}$$

where l is period of the variation of the radius and b is the amplitude of the variation. The average radius of tube m is

$$\bar{r}_m = \sqrt{a_m/\pi}, \tag{13}$$

where a_m is the average transversal area of the tube. The total transversal area of all tubes is then

$$A = \sum_{m=1}^{N} a_m . \tag{14}$$

If a fluid-fluid interface is at a position x_I along tube m, it will generate a capillary pressure drop across it equal to
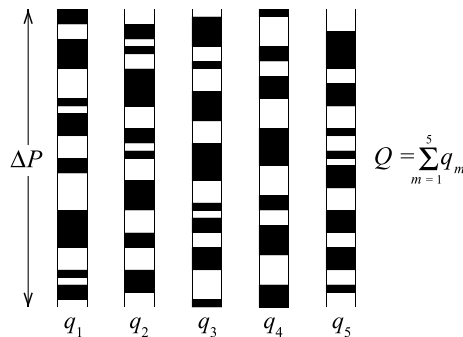

Fig. 1 The capillary bundle model consists of N capillary tubes in parallel. The dark regions signify the non-wetting fluid and the light regions the wetting fluid. The volumetric flow rate in tube m is q_m and the total volumetric flow rate is Q when the pressure drop is ΔP across the tubes. We are not showing the radius modulation along the tubes, see Eq. (12), and we represent the interfaces as being flat

$$p_c(x) = \pm \frac{2\sigma \cos \psi}{\bar{r}_m} \left[1 - b \cos \left(\frac{2\pi}{l} x_I \right) \right] , \tag{15}$$

where σ is the surface tension and ψ is the contact angle. The positive sign is chosen if the wetting fluid is on the $x < x_I$ side of the interface and the negative sign is chosen if the wetting fluid is on the $x > x_I$ side of the interface.

We assume that tube m contains K bubbles of non-wetting fluid. We number the bubbles from $k = 1, ..., K$ in order of their position along the tube. Bubble number k has it midpoint at x_k and its length is Δx_k. Hence, its two interfaces are located at $x = x_k \pm \Delta x_k$.

If we now choose a point $x = x_0$ along the tube and follow it in time, it will obey the equation of motion

$$\dot{x}_0 = -\frac{a_m}{8\pi L\mu_{\text{eff}}} \left[\Delta P + \sum_{k=1}^{K} \sin \left(\frac{\pi}{l} \delta x_k \right) \sin \left(\frac{2\pi}{l} (x_0 + \delta x_k) \right) \right] , \tag{16}$$

where the effective viscosity is given by $\mu_{\text{eff}} = \mu_w + (\mu_n - \mu_w) \sum_{k=1}^{K} (\Delta x_k / L)$. We have defined $\delta x_k = x_k - x_0$. Due to incompressibility, we have that $\delta \dot{x}_k = 0$ for all k. Eq. (16) may be simplified considerably. We define two variables with the units of pressure,

$$\Gamma_{s,m} = \frac{4b\sigma \cos \psi}{\bar{r}_m} \sum_{k=1}^{K} \sin \left(\frac{\pi}{l} \Delta x_k \right) \sin \left(\frac{\pi}{l} \delta x_k \right) , \tag{17}$$

and

$$\Gamma_{c,m} = \frac{4b\sigma \cos \psi}{\bar{r}_m} \sum_{k=1}^{K} \sin \left(\frac{\pi}{l} \Delta x_k \right) \cos \left(\frac{\pi}{l} \delta x_k \right) . \tag{18}$$

From these two variables, we form

$$P_{t,m} = \sqrt{\Gamma_{s,m}^2 + \Gamma_{c,m}^2} . \tag{19}$$

We introduce non-dimensional variables for the chosen point x_0 and time t, $\theta = (2\pi x_0 / L)$ and $\tau = a_m P_{t,m} t / 4Ll\mu_{\text{eff}}$. In these variables, the equation of motion becomes

$$\frac{d\theta}{d\tau} = \frac{\Delta P}{P_{t,m}} - \sin(\theta + \theta_{t,m}) , \tag{20}$$

where $\tan \theta_{t,m} = \Gamma_{s,m} / \Gamma_{c,m}$. This is the equation of motion for the driven over-damped pendulum. We see that $d\theta/d\tau = 0$ if $|\Delta P| \leq P_{t,m}$ and $|d\theta/d\tau| > 0$ if $|\Delta P| > P_{t,m}$. Hence, $P_{t,m}$ is the flow threshold of tube m.

Based on the equation of motion (20), the time-averaged volumetric flow rate in tube m may be calculated,

$$q_m = -\frac{a_m^2}{8\pi \mu_{\text{eff}} L} \text{sgn}(\Delta P) \Theta(|\Delta P| - P_{t,m}) \sqrt{\Delta P^2 - P_{t,m}^2} , \tag{21}$$

where $\text{sgn}(\Delta P)$ is the sign function. We have that

$$Q = \sum_{m=1}^{N} q_m \, , \tag{22}$$

see Fig. 1.

We are now in the position to determine how the threshold pressure for tube m, $P_{t,m}$, scales with L, assuming that we keep the density of bubbles K/L constant. We note that the size of the bubbles Δx_k and their position x_k are random apart from the constraints given by their ordering and that they cannot overlap. This means that the sign of each term in the sums Γ_s and Γ_c, Eqs. (17) and (18), are random. Hence, they sum as uncorrelated random walks. We may therefore interpret $P_{t,m}$, Eq. (19), as the mean square distance covered by the equivalent random walk. As $K \propto L$, we therefore must have that

$$P_{t,m} \sim L^{1/2} \, . \tag{23}$$

A more general version of this argument has been presented in Feder et al. (2022).

So far we have considered only tube m. The flow threshold for the entire bundle is smallest $P_{t,m}$ among the N tubes, i.e.,

$$P_t = \min_{m=1}^{N} P_{t,m} \, . \tag{24}$$

The scaling of $P_{t,m}$ with L will carry over to P_t so that we have

$$P_t \sim L^{1/2} \, . \tag{25}$$

Our next task is to calculate m_β, defined in Eq. (10) for the capillary bundle. The tubes have radii $\bar{r}_m$ drawn from some probability distribution. Since the thresholds $P_{t,m}$ are inversely proportional to $\bar{r}_m$, we consider instead the distribution of thresholds rather than the radii. We furthermore consider the limit of $N \to \infty$.

We follow now (Roy et al. 2019) and define the cumulative probability for the thresholds $P_{t,m}$

$$\Pi(P_{t,m}) = \begin{cases} 0 & \text{if } P_{t,m} \leq P_t \, , \\ \frac{P_{t,m} - P_t}{P_U - P_t} & \text{if } P_t < P_{t,m} \leq P_U \, , \\ 1 & \text{if } P_U < P_{t,m} \, , \end{cases} \tag{26}$$

where we have assumed that $P_t > 0$, which is realistic as $\bar{r}_m$ should always be finite. Here P_t is the threshold pressure defined in Eq. (25). P_U is the threshold pressure at which all tubes flow. This means it is equal to the threshold pressure of the last tube to flow as the pressure difference is increased,

$$P_U = \max_{m=1}^{N} P_{t,m} \, . \tag{27}$$

The scaling of $P_{t,m}$ with L will carry over to P_U so that we have

$$P_U \sim L^{1/2} \, . \tag{28}$$

Averaging over the time-averaged flow rates in each capillary m, Eq. (21), using the cumulative probability (26) gives

$$Q = -\frac{aA\,\text{sign}(\Delta P)}{3\sqrt{2}\pi\mu_{\text{av}}L}\frac{\sqrt{P_t}}{(P_U - P_t)}(|\Delta P| - P_t)^{3/2}\,, \tag{29}$$

for $|\Delta P|$ close to but larger than the threshold P_t. Hence, we find $\beta = 3/2$. The average viscosity is given by $\mu_{\text{av}} = S_w\mu_w + (1 - S_w)\mu_n$, where S_w is the wetting saturation. In terms of the Darcy velocity and pressure gradient, this expression becomes

$$\begin{aligned}v &= -\frac{a\,\text{sign}(p)}{3\sqrt{2}\pi\mu_{\text{av}}}\frac{\sqrt{p_t}}{(p_U - p_t)}(|p| - p_t)^{3/2}\\ &= -m_\beta\,\text{sign}(p)\,(|p| - p_t)^{3/2},\end{aligned} \tag{30}$$

where $p_t = P_t/L$ is the threshold pressure gradient, Eq. (2). Furthermore, we set $p_U = P_U/L$. From Eq. (25), we have that

$$p_t \sim L^{-1/2}\,, \tag{31}$$

and from Eq. (28) that

$$p_U \sim L^{-1/2}\,. \tag{32}$$

Hence, we find that

$$m_\beta \sim L^{1/4}\,. \tag{33}$$

Equations (31) and (33) are two of the main results of this paper.

We are now in the position to determine the scaling on the crossover pressure gradient p_M for the capillary bundle model. By equating Eqs. (7) and (10) for $p = p_M$ and ignoring the threshold pressure gradient p_t by assuming $p_M >> p_t$, we find

$$v = -m_d p_M = -m_\beta p_M^\beta\,. \tag{34}$$

With $\beta = 3/2$ and m_β scaling as in Eq. (33), we find

$$p_M \sim L^{-1/2}\,. \tag{35}$$

Hence, p_M and p_t scale in the same way. They both decrease with increasing L.

4 Numerical Results Based on a Dynamic Pore-Network Model

We base our simulations on the dynamic network simulator described in Aker et al. (1998), Gjennestad et al. (2018), and Sinha et al. (2020). It consists of interfaces in the pores and move according to the pressure gradient they experience. Hence, no wetting films occur in the simulations. We use a square lattice oriented at 45° to the average flow direction. We assume periodic boundary conditions both in the direction orthogonal to the average flow direction and in the direction parallel to the average flow.

The square lattices we have used range in size ($L \times L$) between 48×48 and 208×208. All the links are of length $l = 10^{-3}$ m with its average radius r chosen randomly between $0.1l$ and $0.4l$. The simulation is carried out at both constant flow rate Q and constant pressure gradient ΔP, kept at a certain low value so that the capillary forces dominate

and the relationship between Q and ΔP is a power law. For system sizes $L = 48, 64, 80,$ 96, 112, 128, 144, 160, 176, 192, and 208 we have used, respectively, 20, 20, 15, 15 10, 10, 8, 5, 3, 3, and 3 realizations. We set the surface tension times σ times cosine of the contact angle to the values 0.03 or 0.01 N/m. While calculating the flow rate, instead of assuming a cross section, we summed up the flow rate for all links and divided it by the number of rows in the direction of overall flow.

Figure 2 shows the relation between the pressure gradient and the flow rate when the model reaches the steady state. The upper panels of the figure correspond to constant Q; while, the lower panels show the results for constant ΔP. We show in Fig. 2a pressure difference ΔP as a function of injected pore volumes when keeping Q constant and in figure 2(d) Q as a function of injected pore volumes when keeping ΔP constant. We see that in both cases, within a few injected pore volumes the system reaches a steady state. All data are collected after the system reaches a steady state. For the flow rates shown the system is well within the power law region where Eq. (9) applies.

In order to calculate P_t for a system size L we have adopted two different methods. For the first one we have assumed the mean-field solution from Sinha and Hansen (2012), setting $\beta = 2$ in Eq. (9). For the second method, we keep β free as a fitting parameter and the numerical results are fitted with Eq. (9) with variables P_t, M_β and β. We do not measure the crossover pressure P_M where the power-law relation (9) is replaced by the viscosity-dominated Darcy law (4). It can be estimated using the scaling of p_t and m_β as was done at the end of Sect. 3 and will be done in Sect. 5.
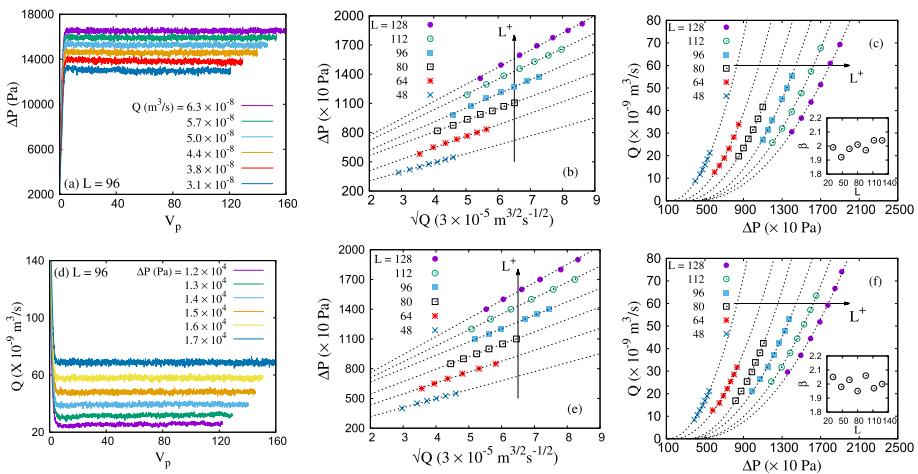

Fig. 2 Upper panel of the figure corresponds to constant flow rate; while, the lower panel corresponds to constant pressure gradient. The size of the network used is 96×96. The saturation S_w value is kept constant at 0.5. **a** and **d** At a constant flow rate ($3.0 \times 10^{-8} < Q < 6.5 \times 10^{-8}$ m^3/s) or pressure gradient ($1.2 \times 10^4 < \Delta P < 1.7 \times 10^4$ Pa), ΔP and Q gradually approaches the steady-state value with increasing pore volumes V_p. **b** and **e** We assume $\beta = 2.0$. The figures show the variation of ΔP with $\sqrt{Q}$ at a constant flow rate (upper) and constant pressure gradient (lower). For both figures the system sizes (L) from up to down are 128, 112, 96, 80, 64, and 48. As the size of the system is increased both the slope of the straight line and the intercept on the ordinate increases. The value of P_t and M_β can be extracted from the intercept of the straight the line on the ordinate and its slope, respectively (see Eq. 36). **c** and **f** β is treated to be a fitting parameter and the numerical results are fitted with Eq. (9) to find β, M_β and P_t. The system sizes used here are the same as **b** and **e**. The fitted β value is observed to be close to 2.0 (shown in the inset).

Constant $\beta = 2$: In the capillary force dominated region, if we assume $\beta = 2$, we get from Eq. (9) that

$$\Delta P \sim \sqrt{\frac{Q}{M_\beta}} + P_t , \tag{36}$$

when taking into account the sign of ΔP used in the simulation. Figure 2b and e show how the pressure gradient ΔP behaves with $\sqrt{Q}$ for constant flow rate and constant pressure gradient, respectively. In both cases, we observe a straight line whose intercept on ordinate gives the value of P_t. As we increase L, the slope of the straight line as well as the intercept P_t increases. M_β can be extracted from the slope of this straight line.

β as fitting parameter: Next, we have kept β as a free parameter and the numerical results are fitted with Eq. (9). The fitted results are shown by dotted lines in Fig. 2c and f. The inset in the same figure shows the β values for different system sizes. The variation in β values show that the mean-field approximation is valid for our numerical results and β has a value close to 2.0.

We now discuss the size effect of the threshold pressure $p_t = P_t/L$. In Fig. 3a we show p_t as a function of L for constant pressure gradient ΔP for the following two cases: $\beta = 2$, as well as when we keep β as an independent fitting parameter. In both cases, a scale-free decay of p_t is observed with L. Figure 3b shows the same power law decay for both constant ΔP and constant flow rate Q with β being treated as an independent fitting parameter. We find in all cases

$$p_t \sim L^{-\alpha} , \tag{37}$$

where $\alpha = 0.55$. This result is in agreement with that found for the capillary bundle model, Eq. (31). We will, however, demonstrate in the following that α depends on the saturation S_w.

Another way of displaying the dependence of the threshold pressure p_t on the system size L is to plot the Darcy velocity v as a function of $p - p_t L^\alpha$. We should then observe data collapse for different values of L. This is precisely what we observe in Fig. 4. We note that whether we keep the pressure drop ΔP or the flow rate Q constant, the results
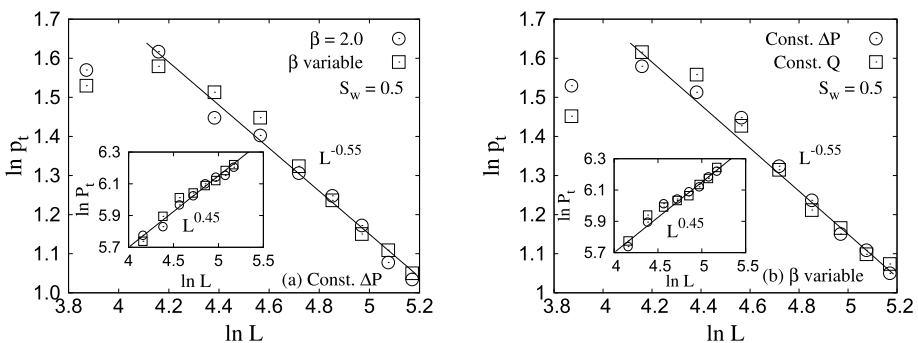

Fig. 3 p_t as a function of L where L ranges from 48 to 176 is shown for **a** constant pressure gradient and $\beta = 2.0$ as well as treating β as a fitting parameter; **b** β as a fitting parameter for both constant pressure and constant flow rate. The inset in both figures shows the size effect for P_t under the same conditions. The saturation $S_w = 0.5$ in all cases
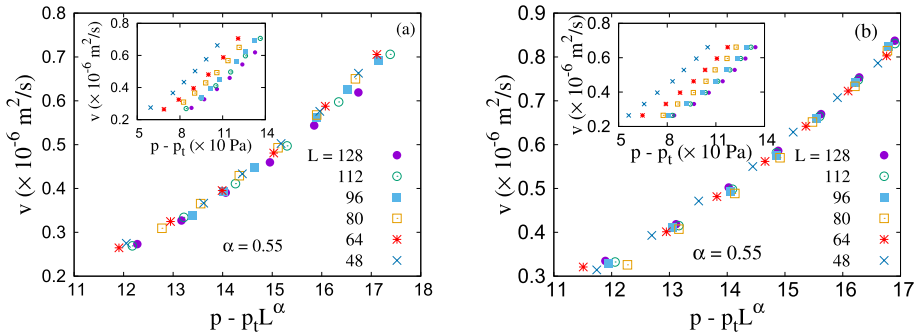
Fig. 4 Darcy velocity $v = Q/L$ plotted against $p - p_t L^\alpha = \Delta P/L - (P_t/L^{1+\alpha})L^\alpha$, where we have set $\alpha = 0.55$, thus producing data collapse. We assumed β to be a fitting parameter. We furthermore set $\mu_n/\mu_w = 1.0$ and $S_w = 0.5$, respectively. The study was carried out for **a** constant pressure gradient and **b** constant flow rate

are quite similar. In light of this behavior, we will only consider the constant pressure drop scenario in the following. We will also in the following keep β as a free parameter.

The dependence of p_t on saturation L for various saturation S_w is shown in Fig. 5. We observe α to remain constant at a low value for $S_w > 0.55$. In the region $0 < S_w < 0.55$, α increases quickly with decreasing saturation. The variation α with S_w is shown in the inset of Fig. 5. In all cases, α is positive so that $p_t \to 0$ as $L \to \infty$.

These results show that the capillary bundle model which predicts $\alpha = 1/2$ does not capture the full mechanisms behind the scaling we observe. We will return to this in the concluding section.

We now turn to the mobility M_β and m_β defined in Eqs. (9) and (11), respectively. Figure 6 shows the size effect for both M_β and m_β.

$$M_\beta \propto L^{-\eta} \tag{38}$$

where η has values 0.78 ($S_w = 0.53$), 0.82 ($S_w = 0.50$) and 0.75 ($S_w = 0.48$), hence the dependence on saturation. From Eq. (11), we have that

$$m_\beta = \frac{M_\beta}{L}L^\beta \sim L^{\beta-1-\eta} = L^\gamma, \tag{39}$$

Fig. 5 Here we show $p_t = P_t/L$ as a function of L for $L = 48$ to $L = 176$, $\mu_n/\mu_w = 1.0$ and for different values of S_w. The behavior is consistent with Eq. (37). The exponent α is a strong function of S_w. However, all values of α are negative so that $p_t \to 0$ as $L \to \infty$
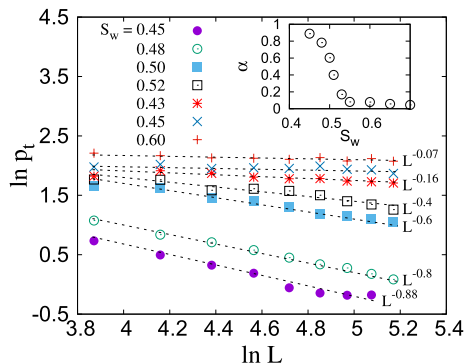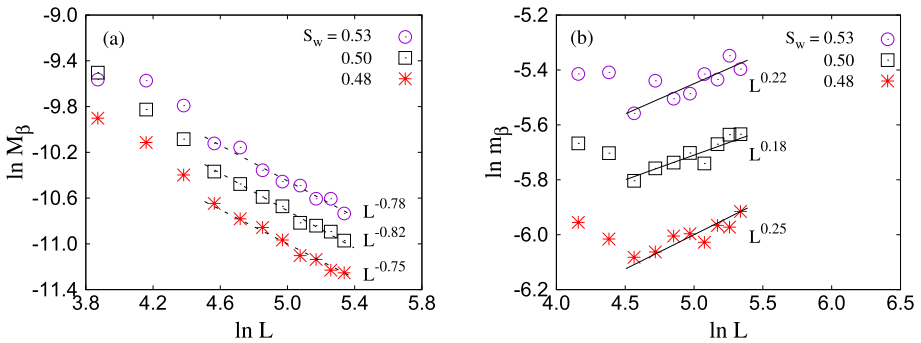
Fig. 6 The mobility M_β defined in Eq. (9) scales with system size L, ranging from $L = 48$ to $L = 208$, as described in Eq. (38). The scaled mobility (11) then scales as $m_\beta = M_\beta L^{\beta-1} \sim L^{\beta-1-\eta}$. Since $\eta < 1$ and $\beta \approx 2.0$, m_β increases with increasing L. We set $\mu_n/\mu_w = 1.0$ here

where we have used that $A = L$ for the two-dimensional networks we use. We have named the combination of exponent $\beta - 1 - \eta = \gamma$. With the value $\beta = 2.0$, we find that $\beta - 1 - \eta$ is larger than zero for all observed η-values. More specifically, we find $\beta - 1 - \eta = 0.22$, 0.18 and 0.25, respectively. We show these results in Fig. 6.

We note how close the exponents measured in Fig. 6b are to the capillary bundle model, Eq. (33), where an exponent 1/4 was found.

5 Discussion and Conclusion

The conclusion we draw from this analysis is that if the power-law mobility m_β, which is defined in Eq. (10) increases with increasing L, the power-law regime vanishes in the continuum limit $L \to \infty$. We repeat the calculation at the end of Sect. 3, but now in a general setting. We assume that the power-law mobility scales as in Eq. (39). By equating Eqs. (7) and (10) for $p = p_M$ and ignoring the threshold pressure gradient p_t by assuming $p_M p_t$, we find

$$m_d p_M = m_\beta p_M^\beta \, , \tag{40}$$

so that

$$p_M \sim L^{-\gamma/(\beta-1)} \, . \tag{41}$$

The exponent $\gamma/(\beta - 1)$ is positive if γ is positive. We have found $\gamma = 1/4$ for the capillary bundle model, Eq. (33) and 0.22 for $S_w = 0.53$, 0.18 for $S_w = 0.50$, and 0.25 for $S_w = 0.48$, see Fig. 6. This means that the crossover pressure p_M separating the power law flow regime from the viscosity-dominated Darcy flow regime decreases with increasing L.

One may illustrate this by sketching the Darcy law (7) as a straight line in a log-log plot of v vs. p as illustrated in Fig. 7. The power-law regime will give another straight line in this diagram with slope β when we ignore the threshold correction $|p| - p_t \to |p|$. The pressure gradient at which they cross each other is p_M. We have $\beta > 1$ so that the two lines cross each other with the power law line below the Darcy line to the left and above to the right. The system follows the lowest of the two lines for any $|p|$. As the power law m_β
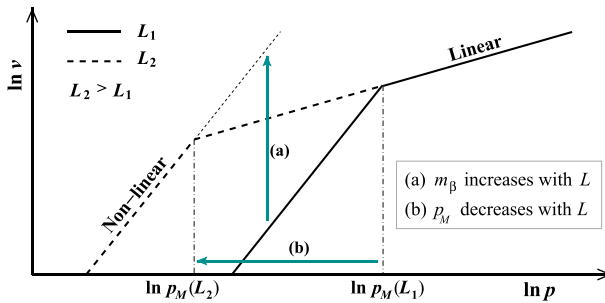
Fig. 7 We show $\ln v$ vs. $\ln p$ in both the linear range, Eq. (7), and the power law range, Eq. (10). Extrapolating the linear part of the curve to $\ln p = 0$, it will cross the $\ln v$ axis at $\ln m_d$, where m_d is the Darcy mobility (8). Extrapolating the power law part of the curve to $\ln p = 0$, it will cross the $\ln v$ axis at $\ln m_\beta$, where m_β is the power-law mobility (11). The linear mobility m_d does not depend on the system size L. The power-law mobility m_β on the other hand *grows* with increasing L, see arrow marked (**a**). This means that the crossover pressure gradient p_M, where the linear and power law part of the curve $\ln v$ vs. $\ln p$ cross moves to the left in the figure, illustrated with arrow (**b**). Hence, p_M decreases with increasing L. We have set the threshold pressure p_t to zero in this figure

mobility increases with increasing L, the cross point between the two lines, p_M, moves to the left, with the result that the power-law regime moves lower values of the pressure gradient p as seen in Fig. 7.

The approach we followed in this paper to reach the conclusion just stated, was first to employed the capillary bundle model which is analytically tractable and then to follow up computationally using the dynamic pore-network model. The capillary bundle model has proved to be an excellent tool to uncover and explain various phenomena encountered in immiscible two-phase flow in porous media. The main results from the use of the capillary bundle model in the present context are given in Eqs. (31) and (33). As the model is analytically tractable, the model explains the mechanism behind the scaling we see.

We find the same qualitative behavior in the dynamic pore-network model we then employ: The threshold pressure p_t shrinks and the mobility m_β increases with increasing system size. Both quantities depend on the system size according to a power law. We find that the exponents depend weakly on the saturation S_w. However, they are roughly similar to the values found in the capillary bundle model.

Our conclusion is that the power law flow regime vanishes in the continuum limit.

We urge that experiments are done in order to move beyond the theoretical and numerical considerations presented here with their obvious limitations.

An understanding of the power law Darcy regime is very important as it occurs right in the parameter range relevant for many industrial situations such as oil recovery, water flow in aquifers etc. It should be noted that all theories for immiscible two-phase flow based on refining the relative permeability approach will be unable to handle this nonlinearity. Hence, it presents a significant challenge to the porous media community.

Declarations

Conflict of interest The authors declare that they have no conflict of interest.

References

Aker, E., Måløy, K.J., Hansen, A., Batrouni, G.G.: A two-dimensional network simulator for two-phase flow in porous media. Transp. Porous Media **32**, 163 (1998). https://doi.org/10.1023/A:1006510106194

Cheon, H.L., Fyhn, H., Hansen, A., Wilhelmsen, Ø., Sinha, S.: Steady-state two-phase flow of compressible and incompressible fluids in a capillary tube of varying radius. Transp. Porous Media **147**, 15 (2023). https://doi.org/10.1007/s11242-022-01893-2

Darcy, H.P.G.: Les Fontaines publiques de la ville de Dijon. Exposition et application des principes à suivre et des formules à employer dans les questions de distribution d'eau, Victor Dalamont, Paris (1856)

Doster, F., Hönig, O., Hilfer, R.: Horizontal flow and capillarity-driven redistribution in porous media. Phys. Rev. E **86**, 016317 (2012). https://doi.org/10.1007/s11242-009-9395-0

Feder, J., Flekkøy, E.G., Hansen, A.: Physics of flow in porous media. Cambridge University Press, Cambridge (2022)

Fyhn, H., Sinha, S., Roy, S., Hansen, A.: Rheology of immiscible two-phase flow in mixed wet porous media: dynamic pore network model and capillary fiber bundle model results. Transp. Porous Media **139**, 491 (2021). https://doi.org/10.1007/s11242-021-01674-3

Fyhn, H., Sinha, S., Hansen, A.: Local statistics of immiscible and incompressible two-phase flow in porous media. Physica A **616**, 128626 (2023). https://doi.org/10.1016/j.physa.2023.128626

Fyhn, H., Sinha, S., Hansen, A.: Effective rheology of immiscible two-phase flow in porous media consisting of random mixtures of grains having two types of wetting properties. Front. Phys. **11**, 1175426 (2023). https://doi.org/10.3389/fphy.2023.1175426

Gao, Y., Lin, Q., Bijeljic, B., Blunt, M.J.: Pore-scale dynamics and the multiphase Darcy law. Phys. Rev. Fluids **5**, 013801 (2020). https://doi.org/10.1103/PhysRevFluids.5.013801

Gjennestad, MAa., Vassvik, M., Kjelstrup, S., Hansen, A.: Stable and efficient time integration of a dynamic pore network model for two-phase flow in porous media. Front. Phys. **6**, 56 (2018). https://doi.org/10.3389/fphy.2018.00056

Gray, W.G., Miller, C.T.: Introduction to the thermodynamically constrained averaging theory for porous medium systems. Springer, Berlin (2014)

Grøva, M., Hansen, A.: Two-phase flow in porous media: power-law scaling of effective permeability. J. Phys.: Conf. Series **319**, 012009 (2011). https://doi.org/10.1088/1742-6596/319/1/012009

Hansen, A., Sinha, S., Bedeaux, D., Kjelstrup, S., Gjennestad, M.A., Vassvik, M.: Relations between seepage velocities in immiscible, incompressible two-phase flow in porous media. Transp. Porous Media **125**, 565 (2018). https://doi.org/10.1007/s11242-018-1139-6

Hansen, A., Flekkøy, E.G., Sinha, S., Slotte, P.A.: A statistical mechanics framework for immiscible and incompressible two-phase flow in porous media. Adv. Water Res. **171**, 104336 (2023). https://doi.org/10.1016/j.advwatres.2022.104336

Hassanizadeh, S.M., Gray, W.G.: Mechanics and thermodynamics of multiphase flow in porous media including interphase boundaries. Adv. Water Res. **13**, 169 (1990). https://doi.org/10.1016/0309-1708(90)90040-B

Hassanizadeh, S.M., Gray, W.G.: Towards an improved description of the physics of two-phase flow. Adv. Water Res. **16**, 53 (1993). https://doi.org/10.1016/0309-1708(93)90029-F

Hassanizadeh, S.M., Gray, W.G.: Thermodynamic basis of capillary pressure in porous media. Water Resour. Res. **29**, 3389 (1993). https://doi.org/10.1029/93WR01495

Hilfer, R.: Capillary pressure, hysteresis and residual saturation in porous media. Physica A **359**, 119 (2006). https://doi.org/10.1016/j.physa.2005.05.086

Hilfer, R.: Macroscopic capillarity and hysteresis for flow in porous media. Phys. Rev. E **73**, 016307 (2006). https://doi.org/10.1103/PhysRevE.73.016307

Hilfer, R.: Macroscopic capillarity without a constitutive capillary pressure function. Physica A **371**, 209 (2006). https://doi.org/10.1016/j.physa.2006.04.051

Hilfer, R., Besserer, H.: Macroscopic two-phase flow in porous media. Physica B **279**, 125 (2000). https://doi.org/10.1016/S0921-4526(99)00694-8

Hilfer, R., Doster, F.: Percolation as a basic concept for capillarity. Transp. Por. Med. **82**, 507 (2009). https://doi.org/10.1007/s11242-009-9395-0

Joekar-Niasar, V., Hassanizadeh, S.M.: Analysis of fundamentals of two-phase flow in porous media using dynamic pore-network models: a review. Crit. Rev. Environ. Sc. Tech. **42**, 1895 (2012). https://doi.org/10.1080/10643389.2011.574101

Kjelstrup, S., Bedeaux, D., Hansen, A., Hafskjold, B., Galteland, O.: Non-isothermal transport of multi-phase fluids in porous media, the entropy production. Front. Phys. **6**, 126 (2018). https://doi.org/10.3389/fphy.2018.00126

Kjelstrup, S., Bedeaux, D., Hansen, A., Hafskjold, B., Galteland, O.: Non-isothermal transport of multi-phase fluids in porous media, constitutive equations. Front. Phys. **6**, 150 (2019). https://doi.org/10.3389/fphy.2018.00150

Lanza, F., Rosso, A., Talon, L., Hansen, A.: Non-Newtonian rheology in a capillary tube with varying radius. Transp. Porous Media **145**, 245 (2022). https://doi.org/10.1007/s11242-022-01848-7

Leverett, M.C.: Capillary behavior in porous solids. Trans. AIMME **142**, 152 (1941). https://doi.org/10.2118/941152-G

Måløy, K.J., Wu, X.L., Hansen, A., Roux, S.: Elastic contact on rough fracture surfaces. Europhys. Lett. **24**, 35 (1993). https://doi.org/10.1209/0295-5075/24/1/006

Niessner, J., Berg, S., Hassanizadeh, S.M.: Comparison of two-phase Darcy's law with a thermo-dynamically consistent approach. Transp. Por. Med. **88**, 133 (2011). https://doi.org/10.1007/s11242-011-9730-0

Pedersen, H., Hansen, A.: Parameterizations of immiscible two-phase flow in porous media. Front. Phys. **11**, 1127345 (2023). https://doi.org/10.3389/fphy.2023.1127345

Rassi, E.M., Codd, S.L., Seymour, J.D.: Nuclear magnetic resonance characterization of the stationary dynamics of partially saturated media during steady-state infiltration flow. New J. Phys. **13**, 015007 (2011). https://doi.org/10.1088/1367-2630/13/1/015007

Roy, S., Hansen, A., Sinha, S.: Effective rheology of two-phase flow in a capillary fiber bundle model. Front. Phys. **7**, 92 (2019). https://doi.org/10.3389/fphy.2019.00092

Roy, S., Sinha, S., Hansen, A.: Flow-area relations in immiscible two-phase flow in porous media. Front. Phys. **8**, 4 (2020). https://doi.org/10.3389/fphy.2020.00004

Roy, S., Pedersen, H., Sinha, S., Hansen, A.: The co-moving velocity in immiscible two-phase flow in porous media. Transp. Porous Media **143**, 69 (2022). https://doi.org/10.1007/s11242-022-01783-7

Scheidegger, A.E.: Theoretical models of porous matter, Producers Monthly, August, 17 (1953)

Scheidegger, A.E.: The physics of flow through porous media. University of Toronto Press, Toronto (1974)

Sinha, S., Hansen, A.: Effective rheology of immiscible two-phase flow in porous media. Europhys. Lett. **99**, 44004 (2012). https://doi.org/10.1209/0295-5075/99/44004

Sinha, S., Hansen, A., Bedeaux, D., Kjelstrup, S.: Effective rheology of bubbles moving in a capillary tube. Phys. Rev. E **87**, 025001 (2011). https://doi.org/10.1103/PhysRevE.87.025001

Sinha, S., Bender, A.T., Danczyk, M., Keepseagle, K., Prather, C.A., Bray, J.M., Thrane, L.W., Seymour, J.D., Codd, S.L., Hansen, A.: Effective rheology of two-phase flow in three-dimensional porous media: experiment and simulation. Transp. Porous Med. **119**, 77–94 (2017). https://doi.org/10.1007/s11242-017-0874-4

Sinha, S., Gjennestad, MAa., Vassvik, M., Hansen, A.: Fluid meniscus algorithms for dynamic pore-network modeling of immiscible two-phase flow in porous media. Front. Phys. **8**, 548497 (2020). https://doi.org/10.3389/fphy.2020.548497

Tallakstad, K.T., Knudsen, H.A., Ramstad, T., Løvoll, G., Måløy, K.J., Toussaint, R., Flekkøy, E.G.: Steady-state two-phase flow in porous media: statistics and transport properties. Phys. Rev. Lett. **102**, 074502 (2009a). https://doi.org/10.1103/PhysRevLett.102.074502

Tallakstad, K.T., Løvoll, G., Knudsen, H.A., Ramstad, T., Flekkøy, E.G., Måløy, K.J.: Steady-state, simultaneous two-phase flow in porous media: an experimental study. Phys. Rev. E **80**, 036308 (2009b). https://doi.org/10.1103/PhysRevE.80.036308

Valavanides, M.S.: Steady-state two-phase flow in porous media: review of progress in the development of the deprof theory bridging pore- to statistical thermodynamics-scales. Oil Gas Sci. Technol. **67**, 787–804 (2012). https://doi.org/10.2516/ogst/2012056

Valavanides, M.S.: Review of steady-state two-phase flow in porous media: independent variables, uni-versal energy efficiency map, critical flow conditions, effective characterization of flow and pore network. Transp. Porous Media **123**, 45–99 (2018). https://doi.org/10.1007/s11242-018-1026-1

Valavanides, M.S., Constantinides, G.N., Payatakes, A.C.: Mechanistic model of steady-state two-phase flow in porous media based on ganglion dynamics. Transp. Porous Media **30**, 267 (1998). https://doi.org/10.1023/A:1006558121674

Wyckoff, R.D., Botset, H.G.: The flow of gas-liquid mixtures through unconsolidated sands. Physics **7**, 325–345 (1936). https://doi.org/10.1063/1.1745402

Xu, X., Wang, X.: Non-Darcy behavior of two-phase channel flow. Phys. Rev. E **90**, 023010 (2014). https://doi.org/10.1103/PhysRevE.90.023010

Yiotis, A.G., Dollari, A., Kainourgiakis, M.E., Salin, D., Talon, L.: Nonlinear Darcy flow dynamics during ganglia stranding and mobilization in heterogeneous porous domains. Phys. Rev. Fluids **4**, 114302 (2019). https://doi.org/10.1103/PhysRevFluids.4.114302

Zhang, Y., Bijeljic, B., Gao, Y., Lin, Q., Blunt, M.J.: Quantification of nonlinear multiphase flow in porous media. Geophys. Res. Lett. **45**, e2020GL090477 (2021). https://doi.org/10.1029/2020GL090477

Zhang, Y., Bijeljic, B., Blunt, M.J.: Nonlinear multiphase flow in hydrophobic porous media. J. Fluid Mech. **934**, R3 (2022). https://doi.org/10.1017/jfm.2021.1148

Zhao, B., MacMinn, C.W., Primkulov, B.K., Chen, Y., Valocchi, A.J., Zhao, J., Kang, Q., Bruning, K., McClure, J.E., Miller, C.T., Fakhari, A., Bolster, D., Hiller, T., Brinkmann, M., Cueto-Felgueroso, L., Cogswell, D.A., Verma, R., Prodanovic, M., Maes, J., Geiger, S., Vassvik, M., Hansen, A., Segre, E., Holtzman, R., Yang, Z., Yuan, C., Chareyre, B., Juanes, R.: Comprehensive comparison of pore-scale models for multiphase flow in porous media. Proc. Natl. Acad. Sci. **116**, 13799 (2019). https://doi.org/10.1073/pnas.1901619116